Mapping electric fields in real nanodevices by operando electron holography

Maria Brodovoi, Kilian Gruel, Aurélien Masseboeuf, Lucas Chapuis, Martin Hÿtch, Frédéric Lorut, Christophe Gatel

▶ **To cite this version:**

Maria Brodovoi, Kilian Gruel, Aurélien Masseboeuf, Lucas Chapuis, Martin Hÿtch, et al.. Mapping electric fields in real nanodevices by operando electron holography. Applied Physics Letters, 2022, 120 (23), pp.233501. 10.1063/5.0092019 . hal-03752638

HAL Id: hal-03752638
https://hal.science/hal-03752638

Submitted on 17 Aug 2022

HAL is a multi-disciplinary open access archive for the deposit and dissemination of scientific research documents, whether they are published or not. The documents may come from teaching and research institutions in France or abroad, or from public or private research centers.

L'archive ouverte pluridisciplinaire **HAL**, est destinée au dépôt et à la diffusion de documents scientifiques de niveau recherche, publiés ou non, émanant des établissements d'enseignement et de recherche français ou étrangers, des laboratoires publics ou privés.

M. Brodovoi, K. Gruel, A. Masseboeuf, L. Chapuis, M. Hÿtch, F. Lorut, and C. Gatel, **Appl. Phys. Lett.** 120, 233501 (2022). *Mapping electric fields in real nanodevices by operando electron holography*. *10.1063/5.0092019*

Mapping electric fields in real nanodevices by *operando* electron holography

Maria Brodovoi[1,2], Kilian Gruel[1], Aurélien Masseboeuf[1], Lucas Chapuis[1], Martin Hÿtch[1], Frédéric Lorut[2], Christophe Gatel[1,3,*]

[1] CEMES-CNRS, 29 rue Jeanne Marvig, 31055, Toulouse, France
[2] STMicroelectronics, 850 rue Jean Monnet, 38920 Crolles, France
[3] University Toulouse III – Paul Sabatier, 118 route de Narbonne, 31062 Toulouse, France

*Corresponding author: christophe.gatel@cemes.fr

Keywords: Transmission electron microscopy, electron holography, focused ion beam sample preparation, Circuit edition, nano-electronic, devices, nanocapacitors, electrical properties, finite element modelling

Abstract

Nano-electronic devices play an essential role in many domains, and their development and improvement attract considerable attention in fundamental and applied research. Access to the local physical processes involved in these nanosystems during their operation is therefore crucial. We show how electric fields in real nanodevices can be studied under working conditions using *operando* electron holography. A specific sample preparation method was first developed to bias electron-transparent nanodevices extracted from production lines whilst ensuring their electrical connectivity and functionality without employing dedicated probe-based holders. Metal-insulator-metal (MIM) nanocapacitors were prepared using this approach based on focused ion beam (FIB) circuit modification. *Operando* electron holography allowed the electric potential to be quantitatively mapped in the active areas, and between devices, whilst biasing the devices *in situ*. Experimental results were compared with finite element method (FEM) modelling simulations to determine local electrical parameters. We demonstrate that electrical properties such as capacitance and surface charge density can be measured at the nanoscale and have been preserved by our sample preparation methodology when compared to macroscopic measurements. This work paves the way for mapping the local electrical properties of more complex biased devices.

Main text

The development of nanometer-scaled electronic devices with reduced dimensions, involving new materials or new architectures such as Magnetic Random Access Memories (MRAM)[1–4], memristors[5–7] or Phase Change Memories (PCM)[8–12], requires a deeper understanding of their operating properties. While electrical and physical characterizations are widely used to monitor and evaluate both the device performance and the quality of the layer stack, there is a lack of knowledge on how the electromagnetic fields are precisely mediated along devices at the nanoscale level. Correlating local electric fields mapped across a chosen device with its structural properties and chemical composition would greatly help research laboratories and the microelectronics industry in the development of new nano-electronic devices. Furthermore, these local studies could also provide methods to determine the root causes of electrical failure[13] to improve the devices in terms of reliability, speed and power consumption.

Transmission Electron Microscopy (TEM) is a powerful technique for studying the properties of individual nanosystems with very high spatial resolution. Among TEM methods, off-axis Electron Holography (EH) is an interferometric technique that allows quantitative mapping of electrical potentials inside and around the specimen, as well as the measurement of charge distributions[14–18] with a precision down to the elementary charge.[19] EH experiments, when combined with *in situ* biasing, pave the way for nanoscale studies of fundamental electrical phenomena of nanodevices in working conditions. However, despite these exciting prospects, *operando* EH has been used relatively little to investigate the local properties of nanosystems. A few model systems (nano tips[20–24] , quantum wells[25], nanowires[26,27], p-n junctions[28–31], oxide layers[32]) have been studied, but key issues such as specimen preparation, surface damage layers, stray field and electron radiation were identified.[30,33,34] The investigation of real devices are rarer still[35,36], even with dedicated probe-based holders.[37] The main problem is that stray fields around the nanoprobe may interfere with the reference wave required in holography[21] and the potential applied to the active area.[38] In addition, the contact resistance between nanoprobe and sample is unknown, poorly controllable and causes mechanical instabilities.

In situ biasing TEM experiments thus necessitate a specific and complex sample preparation that minimizes preparation artifacts whilst ensuring the electrical functionality of the nanodevice itself. A dedicated setup for applying bias from the macroscopic to nanometre scale is also required to avoid electrostatic discharge that can destroy the fragile specimen. Moreover, the signal from local charge distributions is extremely weak and measuring such a signal on a working device prepared by sample

preparation methods such focused-ion beam (FIB) is very challenging. Finally, the analysis of the resulting phase images remains complex due to the integration of the signal along the electron path as well as additional effects (beam-induced charge, stray fields and sample preparation artifacts).

Here we present the methodology that we have been developing for mapping the electrical properties of nano-electronic devices extracted directly from production lines without using a probe-based approach. We investigated the potential distribution at the nanoscale of metal-insulator-metal (MIM) nanocapacitors using advanced FIB sample preparation and state-of-the-art EH. Capacitors are, in fact, one of the most important components in all electronic devices. They are widely used in analog and RF circuit applications for energy storage and delivery in memory devices such as flash memories and random access memory (RAM) chips, and processors whose performance is dependent on their miniaturization and operation. Experimental phase measurements will be compared to additional numerical simulations using finite element modelling (FEM) including factors such as specimen geometry and stray fields.

Our results demonstrate that electrical properties such as electric field, capacitance and surface charge density can be preserved and investigated at the nanoscale.

Experiments were carried out on an array of parallel MIM nanocapacitors extracted from a matrix structure integrated in a STMicroelectronics 28 nm process test chip. The nanocapacitors used in backend upper layers for high frequency circuit applications are made up of a thin 11.5 nm tantalum pentoxide (Ta_2O_5) high-k insulator sandwiched between two TiN electrodes connected to a Cu pillar (above) and a Al layer (below) (Fig. 1). The upper electrode of TiN has a width of 950 nm (in the plane of the image) and 1.7 μm in depth (out-of-plane).

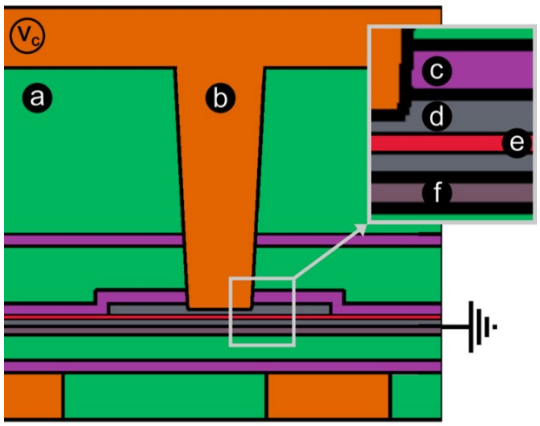

FIG. 1. Architecture of MIM nanocapacitor: (a) SiO_2, (b) Cu interconnects; (c) Si_3N_4; (d) TiN electrodes; (e) active region of Ta_2O_5 dielectric;, (f) Al electrode.

Prior to experiments, individual MIM of the array were measured to have a capacitance of 35±2fF at 1MHz using a nanoprobe (nProber III from ThermoFisher). Assuming the formula for a parallel plate capacitor with a surface area corresponding to the top TiN electrode gives a relative electric permittivity of the thin-layer Ta_2O_5 to be 28±1, which is in the range of values found in the literature.[40]

The specimen-device for holography experiments was prepared using a dual-beam FIB (Helios NanoLab 1200AT DualBeam from ThermoFisher) with a gallium liquid-metal ion source and gas injection system (GIS). A slab of material containing the MIM array was lifted from a fully processed wafer and prepared for electron transparency and *in situ* biasing (Fig. 2).

To ensure proper charge evacuation during specimen navigation and preparation, a thin conductive layer of gold-palladium alloy was deposited on the sample surface prior to extraction. The specimen surface was then connected to the Si substrate by milling a hole in the pad, allowing the charge from the electron beam to drain to the ground. Top and bottom electrodes were also temporarily connected by Pt deposition to prevent electrostatic discharges harming the nanocapacitors during the deprocessing. The specimen-device was then deprocessed top-down with FIB until the copper lines connecting the nanocapacitors were exposed.

A second layer of Pt was deposited to equalize the potential of the two electrodes reconstructing the top circuit, and to protect the structure during further milling. The lamella was then cut and extracted from the wafer and placed on a dedicated chip (Hummingbird Scientific) over a trench surrounded by the prepatterned Au tracks (Fig. 2(a)) before being welded by W deposition using GIS at both ends to ensure the electrical connection (Fig. 2(b)).

Final thinning of the lamella was performed with a low energy ion beam (8 kV) to minimize the impact of surface damage on the thin device compared to the corresponding embedded device. A uniform thickness of about 100 nm was then obtained for two of the capacitors in the array (Figures 2(c) and 2(d)). The final step in the preparation process was to cut trenches so that the top and the bottom electrodes could be biased independently.

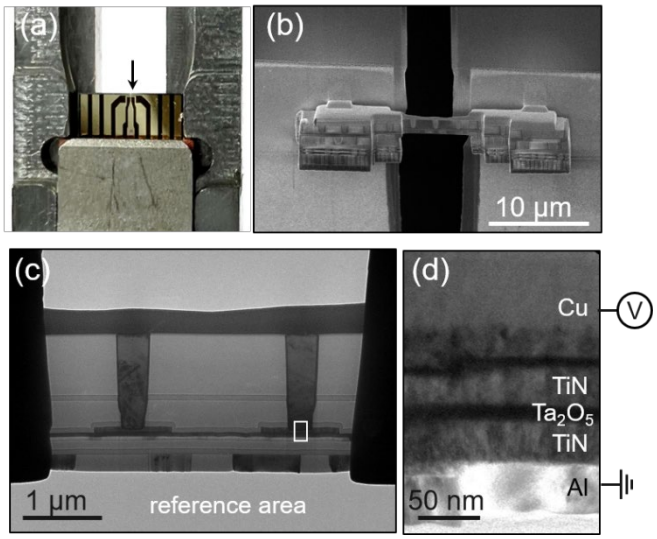

FIG. 2. MIM nanocapacitor specimen-device prepared for operando EH study: (a) chip inserted in sample holder (arrow indicates position of MIM nanocapacitors); (b) SEM image of sample device connected to gold electrodes on chip; (c) TEM image of final specimen-device active area; (d) enlargement of MIM nanocapacitor showing stack.

Such specimen-devices are extremely delicate, with capacitances estimated to be only around 2 fF (the cross-sectional area of the dielectric in the thin lamella is 17 times smaller of the original device). An additional setup consisting of several levels of electrical connections with adapted equipment and software, was therefore developed to protect the thinned nanocapacitors from electrical discharge. Indeed, the electrical resistance of completed specimen-devices was measured prior to TEM experiments to confirm that the nanocapacitors had not been electrically shorted. The chip supporting the connected devices was inserted into a Hummingbird holder designed specifically for biasing experiments (1600 series, Hummingbird scientific) and connected to this additional setup. The bottom electrode was grounded whilst positive, negative or zero biases were applied *in situ* to the top electrode for the electron holography experiments.

The principle of off-axis electron holography is to use an electrostatically charged wire to interfere a beam of highly coherent electrons that has interacted with the specimen, called "object wave", with a reference wave that has not undergone interaction with any field.[41–43] The resulting interference pattern (*i.e.* the hologram) contains all of information on the phase shift of the electron wave experienced when interacting with the local electromagnetic fields.[14,43]

The electrical potential V distribution induces a phase shift ϕ recorded in the *x-y* image plane:[44–46]

$$\phi(x,y) = C_E \int V(x,y,z)dz \qquad (1)$$

where C_E is an energy-related constant that depends on the accelerating voltage (6.526 10^6 $V^{-1}.m^{-1}$ at 300kV) and z the direction of the electron path. V is the sum of the mean internal potential V_{MIP}, which is related to the atomic potential and static charges, and V_{Bias}, which is caused by the applied bias. As a result, ϕ can be divided into two sub-contributions, ϕ_{MIP}, and ϕ_{Bias}. Since ϕ_{MIP} does not depend on the bias, it can be measured by grounding the two electrodes and subtracted from the total measured phase shift. It is then possible to isolate ϕ_{Bias} on applying bias.

Operando EH experiments were carried out on a Hitachi HF3300-C (I2TEM) microscope specifically designed for *in situ* electron interferometry studies. It is equipped with a cold field-emission gun (CFEG) for optimal brightness and an imaging aberration corrector (BCOR from CEOS), which allows on- and off-axis aberrations to be corrected over wide fields of view. Observations were performed with the microscope operating at 300 kV in Lorentz mode with a spatial resolution of 0.5 nm[47], elliptical illumination and 2 post-specimen biprisms to avoid artefacts linked to Fresnel fringes and to allow adjustment of the interference area with respect to the fringe spacing.[48] The reference wave was placed in the field-free region of the vacuum beneath the Al electrode (cf Fig. 2(c)).

A high-speed 4k by 4k camera (OneView, Gatan Inc.) operating at full-frame rate of 25 images per second was used with a temporal integration window of 250 ms, which corresponds to the sum of the frames displayed in the previous 250 ms. Holograms with an interfringe of 1.5 nm (5 pixels) were acquired using dynamic automation[49] and π-shift method[50] over a total exposure time of 120 s each corresponding to the sum of 480 images.

The phase was monitored in real-time during experiments using HoloLive 1.0 (HREM Research Inc.), a plug-in for the image processing package Digital Micrograph (GMS 3.3, Gatan Inc.). In-house scripts and dedicated code implemented within Digital Micrograph were used to analyze the holograms and extract amplitude and phase images during post-processing. A 5th order Butterworth Fourier-space filter centered on the sideband giving a spatial resolution of 3 nm was selected for the amplitude and phase images. To remove the projector and camera distortion-induced phase modulations, a dedicated reference hologram recorded in a vacuum area was used. For each applied bias, a final field of view of 3.5 µm x 1 µm was reconstructed by aligning and combining 3 images.

Figures 3(a) and 3(b) show the experimental amplitude and phase images, respectively, acquired with 0.6 V of bias applied by the power supply. The phase image only contains the electrostatic contribution ϕ_{Bias} from biasing. The mean phase and linear phase ramp measured within the bottom

substrate were subtracted from the whole phase image. Isophase contours with a spacing of 0.25 rad, calculated from the phase image, have been superimposed on the amplitude image.

On biasing, the phase presents a sharp variation across the Ta_2O_5 layer due to the strong local electrical field in the dielectric, but is relatively uniform within the electrodes, as expected. There is also an in-plane stray field between the nanocapacitors due to the finite lateral dimensions of the upper electrodes (zoom in Fig. 3(b)). This weak stray field is clearly visible because of the very long exposure times of our automated holography experiments.[49]

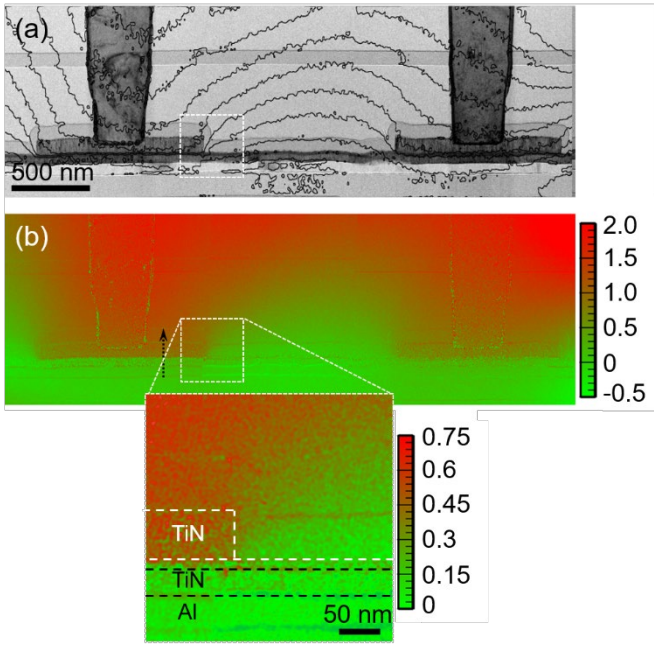

FIG. 3. Operando electron holography:(a) Amplitude image of both MIM nanocapacitors in parallel; (b) Experimental phase image of the induced electrostatic potential for 0.6V bias applied by the power supply.

To analyze quantitatively the potential distribution across the thin oxide layer, profiles were plotted from the phase images along the black arrow (Fig. 3(b)) for different biases and averaged over a width of 50 nm parallel to the interfaces (Fig. 4). The overall phase shift across the dielectric increases linearly with applied bias, as expected from Equation (1). On the other hand, the phase is not completely flat in the electrodes whereas we would expect them to be at a uniform potential.

In fact, the phase curvature is caused by the stray field above and below the thin lamella since the phase is integrated along the whole path of the electron beam (cf Eq. (1)), inside and outside the specimen. Unfortunately, the stray field cannot be described analytically for complex geometries so numerical modeling must be performed to separate the effects of the internal and external fields.

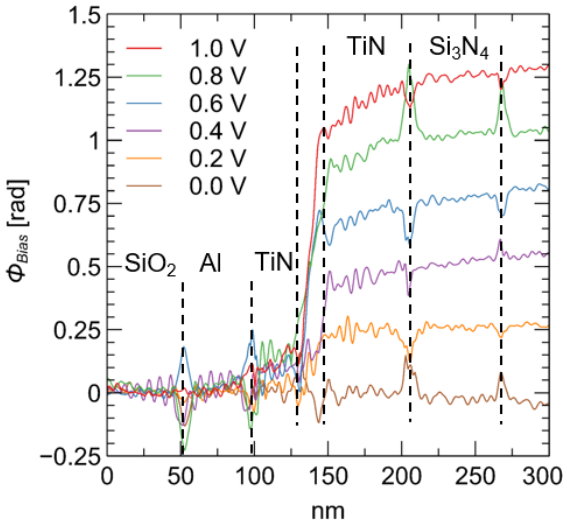

FIG. 4. Phase profiles extracted along the black dotted arrow in Fig. 3(b) for different biases. Ta_2O_5 active layer is between the two TiN electrodes.

Three-dimensional (3D) finite element method (FEM) modeling was performed with the COMSOL software package (COMSOL Multiphysics). The model geometry and dimensions were based on the TEM images of the observed devices, to approach the reality of the experiments as closely as possible. Indeed, this is one of the advantages of TEM experiments that accurate digital twins can be built relatively easily. The main uncertainty is the exact lamella thickness, which we measured by electron energy-loss spectroscopy (EELS) to be 100±10 nm based on theoretical mean-free paths for elastic scattering.

To limit the size of the model, the array of parallel devices was nevertheless limited to four and surrounded by vacuum. From the external boundaries to the active region of the nanocapacitor, the mesh size dynamically adapts to the local dimensions, with a minimum mesh size of about 2 nm. The electrical potential is determined in three dimensions and integrated along the electron path using Eq. (1) to give the 2D phase map. An internal reference is applied in exactly the same way as for the experimental phase images.

The simulated phase corresponding to the experimental case (Fig. 5(a)) is shown in Fig. 5(b) for a lamella thickness of 100 nm. An excellent fit is obtained for the overall phase distribution and for the phase profiles across the active area (Fig. 5(c)). The root mean squared difference between the simulated and experimental phase profiles is only 54 mrad. To convert this into a potential, the phase change across the

dielectric was determined from the simulated curves. The result of 0.88 rad.V^{-1} means that the phase error is equivalent to about 60 mV of applied bias. Simulations also confirm that the out-of-plane stray field is indeed the cause of the non-uniform phase in the region corresponding to the electrodes Even the in-plane stray field is well reproduced (see Fig. 5(d)) and the simulations of the out-of-plane stray field confirm that it is indeed the cause of the non-uniform phase in the region corresponding to the electrodes.

However, in order to obtain this agreement, the local applied bias in the model was 0.40V. Indeed, the dominant source of uncertainty being the lamella thickness, we can estimated the local experimental bias to be within 40 mV of this value. The local bias was therefore significantly lower than the 0.6V indicated by the external power supply. The discrepancy between the bias applied locally and macroscopically is most probably caused by leakage currents and impedances in the connections.

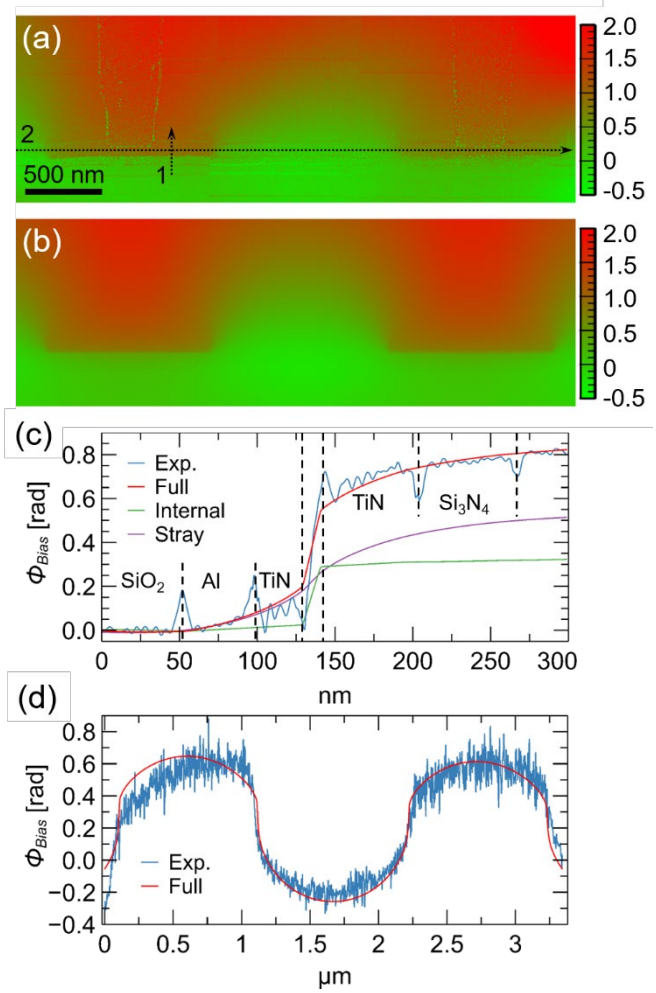

FIG. 5. Quantitative analysis: (a) experimental phase; (b) FEM simulated phase; (c) experimental phase profiles across active layer (black arrow 1), corresponding simulated profiles for the internal field (green), stray field (purple) and total contribution (red); (d) horizontal phase profiles (black arrow 2).

The agreement between simulations and experiment means that we can be confident in the local electrical parameters extracted from the model, such as the electrostatic potential inside the dielectric layer, the capacitance, and surface charge density. The electric field inside the dielectric layer was found to be 0.35±0.04 MVcm^{-1} for the specimen-device with a corresponding capacitance of 2.1 fF, very close to the estimated value from macroscopic measurement, even for the DC bias of the EH experiments. The surface charge density is then 0.12 elementary charge per nm² and per Volt. The energy associated with the induced electrical field between both electrode plates is equal to 3.9 10^{-16} J.V^{-1} , while the energy of the stray fields between two neighboring devices corresponds to 1.24 10^{-18} J.V^{-1}, or 0.3% of the total energy.

These results show that devices extracted from production lines can be prepared for TEM studies whilst preserving their electrical connectivity and functionality. *Operando* electron holography can then be used to quantitatively map the electric potential distribution as a function of bias. That the measured electric field can be modeled with almost no fitting parameters suggests that the device is indeed functioning normally within the microscope.

There is no reason that the same methodology cannot be applied to more complex electronic devices such as MOS transistors or spintronic devices by adapting the sample preparation workflow to achieve a successful circuit modification and enable electrical stimulation of the device. Furthermore, measurements can be correlated to complementary TEM techniques for a full understanding of structural, chemical and electrical properties of individual devices at the nanometer scale. We hope that the ability to study local electric fields quantitatively in newly proposed devices and devices already in production will help efforts to explore fundamental physical processes as well as to develop and improve current devices.

Acknowledgments

We thank Cécile Marcelot, responsible for the microscopy service at CEMES, for help with the EELS analysis. The authors acknowledge the French National Research Agency under the "Investissement d'Avenir" program reference No. ANR-10-EQPX-38-01" and No. 11-IDEX-0002, the "Conseil Regional Midi-Pyrénées" and the European FEDER for financial support within the CPER program. This work was also supported by the French national

project IODA (ANR-17-CE24-0047). This project (ADVENT - 16ENG06) has received funding from the EMPIR program co-financed by the Participating States and from the European Union's Horizon 2020 research and innovation program. The research leading to these results has received funding from the European Union Horizon 2020 research and innovation program under grant agreement No. 823717 – ESTEEM3.

References

[1] J.S. Moodera, L.R. Kinder, T.M. Wong, and R. Meservey, Phys Rev Lett **74**, 3273 (1995).
[2] J.C. Slonczewski, J. Magn. Magn. Mater. **159**, L1 (1996).
[3] J. Åkerman, Science **308**, 508 (2005).
[4] R. Sbiaa, H. Meng, and S.N. Piramanayagam, Phys. Status Solidi RRL – Rapid Res. Lett. **5**, 413 (2011).
[5] L. Chua, IEEE Trans. Circuit Theory 507 (1971).
[6] D.B. Strukov, G.S. Snider, D.R. Stewart, and R.S. Williams, Nature **453**, 80 (2008).
[7] M.D. Ventra and Y.V. Pershin, Nanotechnology **24**, 255201 (2013).
[8] S. Raoux, G.W. Burr, M.J. Breitwisch, C.T. Rettner, Y.C. Chen, R.M. Shelby, M. Salinga, D. Krebs, S.H. Chen, H.L. Lung, and C.H. Lam, IBM J. Res. Dev. **52**, 465 (2008).
[9] S. Raoux, C.T. Rettner, Y.-C. Chen, and G.W. Burr, MRS Bull. **33**, 847 (2008).
[10] D. Krebs, S. Raoux, C.T. Rettner, G.W. Burr, M. Salinga, and M. Wuttig, Appl. Phys. Lett. **95**, 082101 (2009).
[11] G.W. Burr, M.J. Breitwisch, M. Franceschini, D. Garetto, K. Gopalakrishnan, B. Jackson, B. Kurdi, C. Lam, L.A. Lastras, A. Padilla, B. Rajendran, S. Raoux, and R.S. Shenoy, J. Vac. Sci. Technol. B **28**, 223 (2010).
[12] Y. Jung, S.-W. Nam, and R. Agarwal, Nano Lett. **11**, 1364 (2011).
[13] H.J. Engelmann, H. Saage, and E. Zschech, Microelectron. Reliab. **40**, 1747 (2000).
[14] P.A. Midgley and R.E. Dunin-Borkowski, Nat. Mater. **8**, 271 (2009).
[15] M.R. McCartney, N. Agarwal, S. Chung, D.A. Cullen, M.-G. Han, K. He, L. Li, H. Wang, L. Zhou, and D.J. Smith, Ultramicroscopy **110**, 375 (2010).
[16] M. McCartney, R.E. Dunin-Borkowski, and D. Smith, Ultramicroscopy **203**, 105 (2019).
[17] M. Beleggia, T. Kasama, R.E. Dunin-Borkowski, S. Hofmann, and G. Pozzi, Appl. Phys. Lett. **98**, 243101 (2011).
[18] M. Beleggia, T. Kasama, D.J. Larson, T.F. Kelly, R.E. Dunin-Borkowski, and G. Pozzi, J. Appl. Phys. **116**, 024305 (2014).
[19] C. Gatel, A. Lubk, G. Pozzi, E. Snoeck, and M. Hÿtch, Phys. Rev. Lett. **111**, (2013).
[20] Cumings J., Zettl A., McCartney M.R., and Spence J.C.H., Phys Rev Lett **88**, 056804 (2002).
[21] L. de Knoop, F. Houdellier, C. Gatel, A. Masseboeuf, M. Monthioux, and M. Hytch, Micron **63**, 2 (2014).
[22] L. de Knoop, C. Gatel, F. Houdellier, M. Monthioux, A. Masseboeuf, E. Snoeck, and M.J. Hytch, Appl. Phys. Lett. **106**, 263101 (2015).
[23] V. Migunov, C. Dwyer, C.B. Boothroyd, G. Pozzi, and R.E. Dunin-Borkowski, Ultramicroscopy **178**, 48 (2017).
[24] K. He and J. Cumings, Nano Lett. **13**, 4815 (2013).
[25] L.Z.-Y. Liu, C. McAleese, D.V. Sridhara Rao, M.J. Kappers, and C.J. Humphreys, Phys. Status Solidi C **9**, 704 (2012).
[26] M.I. den Hertog, H. Schmid, D. Cooper, J.-L. Rouviere, M.T. Björk, H. Riel, P. Rivallin, S. Karg, and W. Riess, Nano Lett. **9**, 3837 (2009).
[27] M. den Hertog, R. Songmuang, and E. Monroy, J. Phys. Conf. Ser. **471**, 012019 (2013).
[28] K. He, J.-H. Cho, Y. Jung, S.T. Picraux, and J. Cumings, Nanotechnology **24**, 115703 (2013).
[29] A.C. Twitchett, R.E. Dunin-Borkowski, and P.A. Midgley, Phys. Rev. Lett. **88**, 238302 (2002).
[30] S. Yazdi, T. Kasama, M. Beleggia, M. Samaie Yekta, D.W. McComb, A.C. Twitchett-Harrison, and R.E. Dunin-Borkowski, Ultramicroscopy **152**, 10 (2015).
[31] A.C. Twitchett-Harrison, R.E. Dunin-Borkowski, and P.A. Midgley, Scanning **30**, 299 (2008).
[32] Y. Yao, C. Li, Z.L. Huo, M. Liu, C.X. Zhu, C.Z. Gu, X.F. Duan, Y.G. Wang, L. Gu, and R.C. Yu, Nat. Commun. **4**, (2013).
[33] D. Wolf, A. Lubk, A. Lenk, S. Sturm, and H. Lichte, Appl. Phys. Lett. **103**, 264104 (2013).
[34] J.B. Park, T. Niermann, D. Berger, A. Knauer, I. Koslow, M. Weyers, M. Kneissl, and M. Lehmann, Appl. Phys. Lett. **105**, 094102 (2014).
[35] T. Goto, J.S. Jeong, W. Xia, Z. Akase, D. Shindo, and K. Hirata, Microscopy **62**, 383 (2013).
[36] J.F. Einsle, C. Gatel, A. Masseboeuf, R. Cours, M.A. Bashir, M. Gubbins, R.M. Bowman, and E. Snoeck, Nano Res. **8**, 1241 (2015).
[37] N. Ikarashi, H. Takeda, K. Yako, and M. Hane, Appl. Phys. Lett. **100**, 143508 (2012).
[38] M. Duchamp, V. Migunov, A.H. Tavabi, A. Mehonic, M. Buckwell, M. Munde, A.J. Kenyon, and R.E. Dunin-Borkowski, Resolut. Discov. **1**, 27 (2016).
[39] N. Ikarashi, H. Takeda, K. Yako, and M. Hane, Appl. Phys. Lett. **100**, 143508 (2012).
[40] C. Chaneliere, J.L. Autran, R.A.B. Devine, and B. Balland, Mater. Sci. Eng. R Rep. **22**, 269 (1998).
[41] D. Gabor, Nature **161**, 777 (1948).
[42] A. Tonomura, in *Prog. Opt.*, edited by E. Wolf (Elsevier, 1986), pp. 183–220.
[43] A. Tonomura, Rev. Mod. Phys. **59**, 639 (1987).
[44] W. Ehrenberg and R.E. Siday, Proc. Phys. Soc. Sect. B **62**, 8 (1949).
[45] Y. Aharonov and D. Bohm, Phys. Rev. **115**, 485 (1959).
[46] Y. Aharonov and D. Bohm, Phys. Rev. **123**, 1511 (1961).
[47] E. Snoeck, F. Houdellier, Y. Taniguch, A. Masseboeuf, C. Gatel, J. Nicolai, and M. Hytch, Microsc. Microanal. **20**, 932 (2014).
[48] K. Harada, J. Endo, N. Osakabe, and A. Tonomura, E-J. Surf. Sci. Nanotechnol. **6**, 29 (2008).

[49] C. Gatel, J. Dupuy, F. Houdellier, and M.J. Hÿtch, Appl. Phys. Lett. **113**, 133102 (2018).
[50] V.V. Volkov, M.G. Han, and Y. Zhu, Ultramicroscopy **134**, 175 (2013).